
Decoder-only Clustering in Graphs with Dynamic Attributes

Yik Lun Kei¹ Oscar Hernan Madrid Padilla² Rebecca Killick³ James D. Wilson⁴ Chen Xi¹ Robert B. Lund¹

Abstract

This manuscript studies nodal clustering in graphs having a time series at each node. The proposed framework includes priors for low-dimensional representations and a decoder that bridges latent representations with time series. Addressing the limitation that the evolution of nodal attributes is often overlooked, temporal and structural patterns are fused into low-dimensional representations to facilitate clustering. Parameters are learned via maximum approximate likelihood, with a graph-fused LASSO regularization imposed on prior parameters. The optimization problem is solved via alternating direction method of multipliers; Langevin dynamics are employed for posterior inference. Simulation studies on block and grid graphs with autoregressive dynamics, and applications to California county temperatures and a word co-occurrence network demonstrate the effectiveness of the proposed clustering method.

1. Introduction

Networks are used to describe relational phenomena, where entities are denoted by nodes and relations are delineated by edges. Such structures naturally arise in various domains, including social interactions (Snijders, 2011), neurology (Yang et al., 2022), and finance (Jackson & Pernoud, 2021). A fundamental task in network analysis involves partitioning nodes into disjoint sets, where nodes within a set are more connected than nodes in disjoint sets. Such clusters of nodes often provide valuable scientific insights (see Shai et al. (2021) for a collection of case studies). The majority of clustering methods focus on structural patterns (Malliaros & Vazirgiannis, 2013; Abbe, 2018; Macgregor, 2023). However, many networks possess dynamic nodal attributes, and the development of clustering attributed networks is still

in its infancy. This paper demonstrates how to take advantage of nodal time series, providing clustering methods that account for both network structure and attribute dynamics. Section 5 applies the methods to networks with time-varying attributes, including identifying climate regions in California. Both proximities and monthly temperatures are used to develop a realistic clustering of the counties.

Recent advances such as vision–language models highlight the importance of integrating heterogeneous sources of information in a coherent manner. Similarly, clustering nodes of attributed networks demands effective combination of graphical structures and nodal information. Methods have been previously proposed for clustering networks with static attributes. (Binkiewicz et al., 2017) perform covariate-assisted spectral clustering by augmenting the graph Laplacian with pairwise similarities of nodal covariates. (Shen et al., 2024) propose a Bayesian stochastic block model where nodal information is incorporated via a covariate-dependent random partition prior. (Hu & Wang, 2024) leverage individual and neighboring covariates with a node-specific weight matrix to improve clustering. Recently, the graph-fused LASSO regularizations in (Wang et al., 2016), (Chen et al., 2023), and (Madrid Padilla & Chen, 2023) have shown promising results, producing smoothed signals between neighboring nodes, while preserving boundaries between regions having distinct signals. Following (Hallac et al., 2015) and (Yu et al., 2025), our framework adapts the graph-fused LASSO regularization to achieve filtering behavior for clustering.

In many analyses, nodal attributes progress in time, while the network structure remains fixed. Nodal time series can provide valuable clustering information, especially in cases with a non-informative graph such as a grid. Some methods for clustering nodes overlook the evolution of nodal features, flattening temporal patterns into static attributes. An intuitive solution introduces a latent variable at each node. By compressing each nodal series into a low-dimensional latent representation, temporal dynamics can be summarized and then integrated with the structural patterns to facilitate downstream inference. In our approach, latent representations are modeled by node-specific priors, and the latent space is regularized by a graph-fused LASSO penalty to incorporate network information. The resulting low-dimensional representations preserve both graphical structures and attribute dynamics, promoting effective nodal clustering.

¹Department of Statistics, University of California, Santa Cruz
²Department of Statistics and Data Science, University of California, Los Angeles
³School of Mathematical Sciences, Lancaster University
⁴Department of Mathematics and Statistics, University of San Francisco. Correspondence to: Robert Lund <rolund@ucsc.edu>.

Latent space models naturally bridge low-dimensional representations with observed attributes. (Handcock et al., 2007) and (Sewell & Chen, 2015) model nodes in a Euclidean space, by assuming that edge probabilities are greater for node pairs that are closer in the latent space. (Wang et al., 2023) embed both nodes and their attributes in a shared latent space and develop a variational Bayesian EM algorithm to estimate parameters. (Zhu et al., 2023) construct a latent space model for both attractive and repulsive nodes, thereby disentangling network polarization dynamics. In particular, our framework models nodal time series, conditioning on their low-dimensional representations. Unlike a variational auto-encoder (Kingma & Welling, 2014; Kipf & Welling, 2016), which encourages the approximate posterior to align with a zero-mean Gaussian prior, we focus on learning the Gaussian prior means to facilitate clustering. With graph-fused LASSO regularization imposed on the differences between the prior parameters over edges, nodes having similar evolving patterns are encouraged to have similar prior parameters in Euclidean spaces. Consequently, the k -means method that clusters via centroids is well-suited in the resulting low-dimensional latent space.

This manuscript makes the following contributions:

- A decoder-only latent space model is proposed to link the nodal series and latent variables. Anchored on the decoder, the latent variables are regarded as low-dimensional representations of the nodal series, while also capturing network structural patterns. The prior parameters are clustered via k -means method.
- We show how to learn the Gaussian prior parameters in our latent representation. Specifically, our graph-fused LASSO regularization encourages sparsity in the multivariate parameters across edges. This produces similar parameters in neighboring nodes while preserving regions with disparate signals.
- The associated optimization problem is solved via alternating direction method of multipliers (ADMM) with posterior inference. Through simulations on block and grid graphs with autoregressive dynamics, and applications to California county temperatures and a word co-occurrence network, the effectiveness of the proposed framework is demonstrated.

The rest of the manuscript is organized as follows. Section 2 describes our proposed framework. Section 3 presents an objective function with a graph-fused LASSO regularization and develops the ADMM procedure to solve the optimization problem. Section 4 discusses nodal clustering and model selection. Section 5 illustrates the proposed method through simulations and real-data applications. Section 6 discusses limitations and ideas for future work.

2. Decoder-only Latent Space Models

2.1. Model Specification

We consider an undirected graph $\mathcal{G} = (\mathcal{V}, \mathcal{E})$, where \mathcal{V} and \mathcal{E} are the respective node and edge sets. For each node $i \in \mathcal{V}$, let $\{Y_{t,i}\}_{t=1}^n$ denote a sequence of univariate random variables. The node i series is represented as $\mathbf{Y}_i := (Y_{1,i}, Y_{2,i}, \dots, Y_{n,i})^\top$. For each $\mathbf{Y}_i \in \mathbb{R}^n$, we assume existence of a latent variable $\mathbf{Z}_i \in \mathbb{R}^d$ such that \mathbf{Y}_i is generated from \mathbf{Z}_i with the following time series decoder:

$$\mathbf{Y}_i | \mathbf{Z}_i \sim P_\phi(\mathbf{Y}_i | \mathbf{Z}_i) \stackrel{\mathcal{D}}{=} \mathcal{N}(\mathbf{h}_\phi(\mathbf{Z}_i), \mathbf{I}_n),$$

where $\mathbf{h}_\phi : \mathbb{R}^d \rightarrow \mathbb{R}^n$ is a neural network parameterized by ϕ and is elaborated in Section 2.2. Here, $P_\phi(\mathbf{Y}_i | \mathbf{Z}_i)$ is the conditional probability density function of \mathbf{Y}_i given \mathbf{Z}_i . We impose a prior distribution on the latent \mathbf{Z}_i via

$$\mathbf{Z}_i \sim P_{\mu_i}(\mathbf{Z}_i) \stackrel{\mathcal{D}}{=} \mathcal{N}(\mu_i, \mathbf{I}_d).$$

The prior parameter, $\mu_i \in \mathbb{R}^d$, is learned for each node. For the decoder $P_\phi(\mathbf{Y}_i | \mathbf{Z}_i)$, the latent variable $\mathbf{Z}_i \in \mathbb{R}^d$ is a low-dimensional representation of $\mathbf{Y}_i \in \mathbb{R}^n$ at node i .

Figure 1 overviews our framework. The shaded circles in the top layer depict the series $\{\mathbf{Y}_i\}_{i \in \mathcal{V}}$, and the dashed circles in the bottom layer depict the latent $\{\mathbf{Z}_i\}_{i \in \mathcal{V}}$. The series are generated from the latent variables in a bottom-up manner. The decoder $P_\phi(\mathbf{Y}_i | \mathbf{Z}_i)$ with neural network parameter ϕ is shared across all nodes, while the means $\mathbf{h}_\phi(\mathbf{Z}_i)$ differ by nodes. Intuitively, the decoder $P_\phi(\mathbf{Y}_i | \mathbf{Z}_i)$ helps learn the time series representation $\mathbf{Z}_i \in \mathbb{R}^d$ in a top-down manner. The simplicity of the proposed framework is noted, without the need for an encoder.

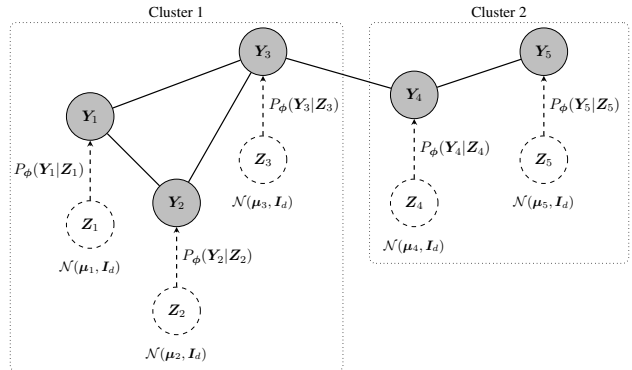


Figure 1. An illustration of our prior distributions and a decoder on a graph with five nodes and two clusters.

2.2. Neural Decoder and Temporal Dependence

The distribution of interest is the marginal $P(\mathbf{Y}_i)$, which is often complicated. Instead of imposing a parametric form directly on the marginal $P(\mathbf{Y}_i)$, our framework introduces

an auxiliary latent variable $\mathbf{Z}_i \in \mathbb{R}^d$ to model $P(\mathbf{Y}_i)$ from a mixture:

$$P(\mathbf{Y}_i) = \int P_\phi(\mathbf{Y}_i|\mathbf{Z}_i)P_{\mu_i}(\mathbf{Z}_i)d\mathbf{Z}_i \quad (1)$$

with the following remarks.

Remark 2.1. The Gaussian assumption is placed on the conditional $P(\mathbf{Y}_i|\mathbf{Z}_i)$, instead of the marginal $P(\mathbf{Y}_i)$. The induced distribution of $P(\mathbf{Y}_i)$ can be highly non-Gaussian and depends on $\mathbf{h}_\phi(\cdot)$.

Remark 2.2. Our framework assumes that $Y_{t,i}$ is independent in time t conditional on \mathbf{Z}_i . Here, $\mathbf{Z}_i \in \mathbb{R}^d$ serves as a low-dimensional representation that captures temporal relationships while retaining a flexible marginal for $P(\mathbf{Y}_i)$. In particular, the covariance of $\mathbf{Y}_i \in \mathbb{R}^n$ is

$$\begin{aligned} \text{Cov}(\mathbf{Y}_i) &= \mathbb{E}[\text{Cov}(\mathbf{Y}_i|\mathbf{Z}_i)] + \text{Cov}[\mathbb{E}(\mathbf{Y}_i|\mathbf{Z}_i)] \\ &= \mathbf{I}_n + \text{Cov}[\mathbf{h}_\phi(\mathbf{Z}_i)] \end{aligned}$$

which depends on $\mathbf{h}_\phi(\cdot)$, thereby allowing for potentially complex marginal temporal dependence.

Remark 2.3. The negative log-likelihood of (1) that involves latent \mathbf{Z}_i is lower bounded (Mattei & Frellsen, 2018):

$$-\ln(P(\mathbf{Y}_i)) \geq \frac{n}{2} \ln(2\pi),$$

rendering associated minimization problems meaningful.

For flexibility of the marginal $P(\mathbf{Y}_i)$, the mean $\mathbf{h}_\phi(\cdot)$ in the decoder $P_\phi(\mathbf{Y}_i|\mathbf{Z}_i)$ is parameterized by a three-layer ReLU neural network, which have universal approximation properties (Hornik et al., 1989; Hornik, 1991; Yarotsky, 2017). This parameterization is particularly chosen for representation learning to capture temporal patterns, yielding node-level representations tailored for clustering and graph-based regularization. In contrast, recurrent-based neural networks are typically designed to model conditional dynamics and are optimized for sequential forecasting tasks, making the latent representations less amenable to node-level abstraction for graph related tasks. Furthermore, recurrent-based neural networks are often computationally more demanding, jeopardizing the optimization procedure elaborated in Section 3. While other architectures can be used, ReLU neural networks have been extensively studied and is well suited for the proposed clustering framework.

3. Learning and Inference

This section develops methods to learn the graph and series structures. A penalized likelihood is formulated first; the resulting constrained optimization is then solved with an ADMM algorithm. Denote the joint log-likelihood of $\{\mathbf{Y}_i\}_{i \in \mathcal{V}}$ as $L(\phi, \mu) = \sum_{i \in \mathcal{V}} \ell(\phi, \mu_i)$, where the node i

marginal log-likelihood is

$$\ell(\phi, \mu_i) = \ln \left(\int P_\phi(\mathbf{Y}_i|\mathbf{Z}_i)P_{\mu_i}(\mathbf{Z}_i)d\mathbf{Z}_i \right).$$

To facilitate clustering of the prior parameters, the penalized optimization

$$\hat{\phi}, \hat{\mu} = \arg \min_{\phi, \mu} \left[-L(\phi, \mu) + \lambda \sum_{(i,j) \in \mathcal{E}} \|\mu_i - \mu_j\|_2 \right] \quad (2)$$

is considered, where $\lambda > 0$ is a tuning parameter for the penalty term. The i th row of the $\mathbb{R}^{N \times d}$ matrix μ is denoted by $\mu_i \in \mathbb{R}^d$, where $N := |\mathcal{V}|$.

The graph-fused LASSO regularization manages associations between nodes, incorporating structural information into our latent representations. The regularization here is a total variation sum of the multivariate pairwise differences $\mu_i - \mu_j \in \mathbb{R}^d$ over edges $(i, j) \in \mathcal{E}$. Our regularization induces sparsity in the differences while permitting simultaneous shifts across nodes. By penalizing the total variation of the prior parameters across edges, our framework can identify meaningful boundaries between clusters having disparate signals.

To optimize (2) which involves latent variables, we first manipulate the objective function. Introduce the slack variables $\nu_{i,j} \in \mathbb{R}^d$ and recast the constrained optimization as

$$\begin{aligned} \hat{\phi}, \hat{\mu} &= \arg \min_{\phi, \mu} \left[-L(\phi, \mu) + \lambda \sum_{(i,j) \in \mathcal{E}} \|\nu_{i,j}\|_2 \right], \quad (3) \\ \text{subject to} \quad &\mu_i - \mu_j = \nu_{i,j}. \end{aligned}$$

The augmented Lagrangian is formulated as

$$\begin{aligned} \mathcal{L}(\phi, \mu, \nu, \rho) &= -L(\phi, \mu) + \lambda \sum_{(i,j) \in \mathcal{E}} \|\nu_{i,j}\|_2 + \\ &\sum_{(i,j) \in \mathcal{E}} \rho_{i,j}^\top (\mu_i - \mu_j - \nu_{i,j}) + \frac{\gamma}{2} \sum_{(i,j) \in \mathcal{E}} \|\mu_i - \mu_j - \nu_{i,j}\|_2^2, \end{aligned}$$

where $\rho_{i,j} \in \mathbb{R}^d$ is the Lagrange multiplier for each $(i, j) \in \mathcal{E}$ and $\gamma > 0$ is an additional penalty parameter for the augmentation term. Let $\mathbf{w}_{i,j} = \gamma^{-1} \rho_{i,j} \in \mathbb{R}^d$ denote the scaled dual variable. The augmented Lagrangian can be equivalently formulated as

$$\begin{aligned} \mathcal{L}(\phi, \mu, \nu, \mathbf{w}) &= -L(\phi, \mu) + \lambda \sum_{(i,j) \in \mathcal{E}} \|\nu_{i,j}\|_2 + \\ &\frac{\gamma}{2} \sum_{(i,j) \in \mathcal{E}} (\|\mu_i - \mu_j - \nu_{i,j} + \mathbf{w}_{i,j}\|_2^2 - \|\mathbf{w}_{i,j}\|_2^2). \end{aligned}$$

An ADMM procedure (Boyd et al., 2011; Wang et al., 2019)

recursively solves our optimization:

$$\begin{aligned} \phi^{(a+1)} &= \arg \min_{\phi} \left[-L(\phi, \boldsymbol{\mu}^{(a)}) \right], \\ \boldsymbol{\mu}_i^{(a+1)} &= \arg \min_{\boldsymbol{\mu}_i} \left[-L(\phi^{(a+1)}, \boldsymbol{\mu}_i) + \right. \end{aligned} \quad (4)$$

$$\left. \frac{\gamma}{2} \sum_{j \in \mathcal{B}(i)} \|\boldsymbol{\mu}_i - \boldsymbol{\mu}_j - \boldsymbol{\nu}_{i,j}^{(a)} + \boldsymbol{w}_{i,j}^{(a)}\|_2^2 \right], \quad \forall i \in \mathcal{V},$$

$$\boldsymbol{\nu}_{i,j}^{(a+1)} = \arg \min_{\boldsymbol{\nu}_{i,j}} \left[\lambda \|\boldsymbol{\nu}_{i,j}\|_2 + \right. \quad (5)$$

$$\left. \frac{\gamma}{2} \|\boldsymbol{\mu}_i^{(a+1)} - \boldsymbol{\mu}_j^{(a+1)} - \boldsymbol{\nu}_{i,j} + \boldsymbol{w}_{i,j}^{(a)}\|_2^2 \right], \quad \forall (i, j) \in \mathcal{E},$$

$$\boldsymbol{w}_{i,j}^{(a+1)} = \boldsymbol{\mu}_i^{(a+1)} - \boldsymbol{\mu}_j^{(a+1)} - \boldsymbol{\nu}_{i,j}^{(a+1)} + \boldsymbol{w}_{i,j}^{(a)}, \quad \forall (i, j) \in \mathcal{E}.$$

Here, a denotes the ADMM algorithm iteration and $\mathcal{B}(i) := \{j \in \mathcal{V} : (i, j) \in \mathcal{E}\}$ is the set of node i 's neighbors.

The solution $\boldsymbol{\mu}_i$ at a particular iteration of the ADMM procedure is

$$\boldsymbol{\mu}_i = \frac{1}{(1 + \gamma|\mathcal{B}(i)|)} \left[\mathbb{E}(\mathbf{Z}_i | \mathbf{Y}_i) + \gamma \sum_{j \in \mathcal{B}(i)} (\boldsymbol{\mu}_j + \boldsymbol{\nu}_{i,j} - \boldsymbol{w}_{i,j}) \right]. \quad (6)$$

Moreover, the gradient with respect to the decoder parameter is

$$-\nabla_{\phi} L(\phi, \boldsymbol{\mu}) = -\sum_{i \in \mathcal{V}} \mathbb{E} \left(\nabla_{\phi} \ln(P(\mathbf{Y}_i | \mathbf{Z}_i)) \middle| \mathbf{Y}_i \right). \quad (7)$$

The parameter ϕ is updated via back-propagation. The update in (5) is equivalent to solving a group LASSO problem (Yuan & Lin, 2006; Vert & Bleakley, 2010; Alafiz et al., 2013). One can update $\boldsymbol{\nu}_{i,j}$ for each edge $(i, j) \in \mathcal{E}$ via

$$\boldsymbol{\nu}_{i,j} = \left(1 - \frac{\lambda}{\gamma \|\mathbf{s}_{i,j}\|_2} \right)_+ \mathbf{s}_{i,j}, \quad (8)$$

where $\mathbf{s}_{i,j} = \boldsymbol{\mu}_i - \boldsymbol{\mu}_j + \boldsymbol{w}_{i,j}$ and $(x)_+ = \max(0, x)$.

Calculating (6) and the gradient in (7) requires evaluating a conditional expectation under the posterior density $P(\mathbf{Z}_i | \mathbf{Y}_i) \propto P(\mathbf{Y}_i | \mathbf{Z}_i) \times P(\mathbf{Z}_i)$. Here, Langevin dynamics are employed to sample from the posterior distribution, approximating conditional expectations (Du & Mordatch, 2019; Nijkamp et al., 2020; Purohit et al., 2024). In particular, let k be the time step of the Langevin dynamics and let $\delta > 0$ be a small step size. The Langevin dynamics to draw samples from the posterior distribution iterate

$$\begin{aligned} \mathbf{Z}_i^{k+1} &= \mathbf{Z}_i^k + \delta [\nabla_{\mathbf{Z}_i} \ln(P_{\phi}(\mathbf{Y}_i | \mathbf{Z}_i^k)) \\ &\quad - (\mathbf{Z}_i^k - \boldsymbol{\mu}_i)] + \sqrt{2\delta} \boldsymbol{\epsilon} \end{aligned} \quad (9)$$

in k , where $\boldsymbol{\epsilon} \sim \mathcal{N}(\mathbf{0}, \mathbf{I}_d)$ is a random perturbation to the process. The gradient of $P_{\phi}(\mathbf{Y}_i | \mathbf{Z}_i)$ with respect to the latent variable \mathbf{Z}_i is calculated through back-propagation. The derivations of the updates and computation complexity of the ADMM procedure are provided in the Appendix.

4. Nodal Clustering and Model Selection

4.1. Nodal Clustering

For graphs with dynamic attributes, time series observed at neighboring nodes often exhibit similar evolving patterns. To capture this behavior, the proposed framework jointly models temporal dynamics and graphical structures, allowing the learned priors to integrate both sources of information. Specifically, the graph-fused LASSO regularization encourages adjacent nodes with similar temporal behavior to have similar prior means, effectively promoting piecewise-constant structure over the graph. The estimated prior means form well-separated regions in a low-dimensional Euclidean space. Therefore, k -means method is applied to $\{\hat{\boldsymbol{\mu}}_i\}_{i \in \mathcal{V}}$, as centroid-based clustering method align well with the geometry induced by the regularization. The resulting partitions are more informative, in the sense that they reflect both temporal similarity and structural proximity, rather than solely relying on the time series $\{\mathbf{Y}_i\}_{i \in \mathcal{V}}$ or the graph structure $\mathcal{G} = (\mathcal{V}, \mathcal{E})$ alone.

Since k -means algorithm requires the number of clusters k , we estimate this parameter via a silhouette score. A range of k in $\{2, \dots, K\}$ is considered; the one having the highest silhouette score $S \in [-1, 1]$, defined by

$$S = \frac{1}{|\mathcal{V}|} \sum_{i \in \mathcal{V}} \frac{d_i^{\text{out}} - d_i^{\text{in}}}{\max(d_i^{\text{in}}, d_i^{\text{out}})},$$

is selected. Here, d_i^{in} is the mean distance between point i and all points in the same cluster, and d_i^{out} is the minimum mean distance between point i and any other cluster. A higher S suggests more cohesive clusters, with distinct separation between different clusters.

4.2. Model Selection

The optimization problem in (3) involves the tuning parameter λ . Given a list of candidate λ values, model selection is performed through cross validation. Specifically, the observed data is split into training and testing sets via nodes. Let $\mathcal{V}_{\text{test}}$ be the node set of the testing data. During training, we replace the node i data \mathbf{Y}_i with the element-wise average $\bar{\mathbf{Y}}_i$ from all neighbors. The node i data is held out for testing when $i \in \mathcal{V}_{\text{test}}$.

After parameters are learned from the training data, $\hat{\boldsymbol{\mu}}$ is used for parameters at removed nodes and the decoder calculates the log-likelihood of the non-training data. The λ with the highest log-likelihood is selected. In particular, the log-likelihoods for the testing data are calculated by

$$\sum_{i \in \mathcal{V}_{\text{test}}} \ln(P(\mathbf{Y}_i)) \approx \sum_{i \in \mathcal{V}_{\text{test}}} \ln \left[\frac{1}{s} \sum_{u=1}^s [P(\mathbf{Y}_i | \mathbf{Z}_{u,i})] \right]$$

where $\{\mathbf{Z}_{u,i}\}_{u=1}^s$ are samples drawn from the marginal

$P_{\hat{\mu}_i}(\mathbf{Z}_i)$ with the learned parameter $\hat{\mu}_i$ for a node i . Eventually, with the selected λ , we learn the model parameters again via the full data, resulting in the final estimated parameters for clustering.

5. Experiments

5.1. Simulations

To generate realistic networks, block and grid graphs will be simulated. Block graphs mimic social relations, where individuals with similar attributes often form cohesive clusters. Grid graphs imitate spatial aspects such as urban layouts or power systems, where entities reside on a lattice and clusters reflect spatial regions. To simulate realistic cluster-specific time series, autoregressive (AR) and vector autoregressive (VAR) models are used. Both models inject temporal dependence by linearly regressing on past series values.

Our simulations generate 50 graph realizations with a varying number of nodes $N := |\mathcal{V}|$. The series length $n = 100$ is used at every node. To evaluate performance, the following standard clustering metrics are considered: normalized mutual information (NMI), adjusted Rand index (ARI), accuracy score (ACC), homogeneity (HOM), completeness (COM), and cluster purity (PUR). These evaluation metrics require a known truth to measure from; see (Emmons et al., 2016) and (Su et al., 2022) for additional details. Six competitors, k -means, dynamic time warping (DTW) (Sakoe & Chiba, 2003), covariate assisted spectral clustering (CASC) (Binkiewicz et al., 2017), semi-definite programming (SDP) (Yan & Sarkar, 2021), spectral clustering on network-adjusted covariates (NAC) (Hu & Wang, 2024), and spectral clustering on ratios-of-eigenvectors (SCORE) (Jin, 2015), are provided for comparison.

The k -means and DTW methods only use the series for clustering, while the SCORE method only uses graphical structure. The CASC, SDP, and NAC are hybrid methods utilizing both series and graphical structures to cluster nodes, similar to our method. Our simulations assess whether integrating both sources of information leads to better clustering than approaches that use the graph or attributes alone; then performances against the hybrid approaches are compared. Details of the competitors are provided in the Appendix.

Throughout, our method is dubbed GFL. The latent dimension is taken as $d = 3$, and the two hidden layers of the neural network each contain 32 neurons. The tuning λ 's are $\{0.1, 0.25, 0.5, 0.75, 1.0\}$ and 10% of the series was held out for model selection. For each λ , 50 iterations of the ADMM procedure are run and $\gamma = \lambda$ is taken. In each ADMM iteration, the neural network is trained using 20 steps of an Adam optimizer with a learning rate of 10^{-4} . For Langevin dynamic sampling, we take $\delta = 0.4$ and 500 samples are drawn for each node using 50 MCMC iterations.

The results for varying latent dimensions as a sensitivity analysis are presented in the Appendix.

Scenario 1

Our first scenario simulates graphs with block structures to demonstrate nodal clustering. Specifically, for the node set \mathcal{V} of size $N := |\mathcal{V}|$, a probability matrix $\mathbf{P} \in [0, 1]^{N \times N}$ is first defined as

$$P_{ij} = \begin{cases} 0.30, & i, j \in C_k, k \in \{1, 2, 3\}, \\ 0.15, & \text{otherwise,} \end{cases}$$

where C_1, C_2, C_3 are three clusters that partition the node set \mathcal{V} . Then edges are sampled via an adjacency matrix format as $A_{i,j} \sim \text{Bernoulli}(P_{i,j})$. For $N = 120$ nodes, our three unbalanced cluster sizes are 30, 40 and 50; for $N = 210$, the cluster sizes are 60, 70, and 80.

For node i in cluster C_k , its time series $\mathbf{Y}_i = \{Y_{t,i}\}_{t=1}^T$ is generated via a cluster-specific AR model of order one:

$$Y_{t,i} = \mu_k + \psi_k(Y_{t-1,i} - \mu_k) + \varepsilon_{t,i}, \quad t = 2, \dots, T, \quad i \in C_k,$$

where μ_k is the mean of cluster C_k , ψ_k is the AR coefficient with $|\psi_k| < 1$, and $\varepsilon_{t,i} \sim \mathcal{N}(0, 1)$ is Gaussian white noise. The process is rendered stationary by taking the initial state

$$Y_{1,i} \sim \mathcal{N}\left(\mu_k, \frac{\sigma_k^2}{1 - \psi_k^2}\right), \quad i \in C_k. \quad (10)$$

We choose $\psi_k = 0.5$ and $\sigma_k^2 = 1$ for all three clusters. Cluster means are $\mu_1 = -1.0$, $\mu_2 = 0.0$, and $\mu_3 = 1.0$. Figure 2 depicts a simulated block graph and its associated series means. Table 1 reports sample means and standard deviations of our clustering evaluation metrics.

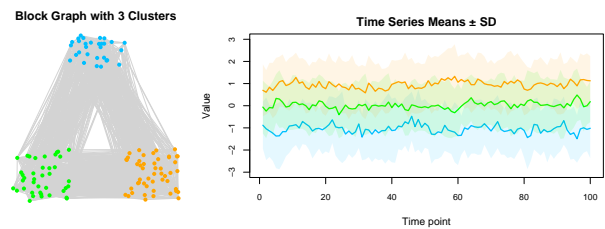


Figure 2. A simulated graph and its time series sample means. The left plot is a simulated graph with unbalanced cluster sizes and 120 nodes. The right plot shows time series sample means along with the ± 1 standard deviation bands at each time point for the clusters.

With 120 nodes, k -means applied directly to the series performs reasonably well. This is because the clusters are well separated via their series means. The graph-based methods, such as CASC, SDP, NAC, and SCORE, do not perform as well, which is attributed to small graph sizes and unbalanced cluster sizes. As N increases from 120 to 210, the performance of these methods improve, which is expected since

more data is available. The DTW method also improves, and the graph-based methods benefit from a larger adjacency matrix in their spectral clusterings. Importantly, our proposed GFL method outperforms all competitor methods, highlighting its utility.

Table 1. Sample means (one standard deviation) of our evaluation metrics for Scenario 1. The best metric is in bold.

N	METHOD	NMI \uparrow	ARI \uparrow	ACC \uparrow	HOM \uparrow	COM \uparrow	PUR \uparrow
120	GFL $_{d=3}$	98.52% (0.03)	98.96% (0.02)	99.63% (0.01)	98.49% (0.03)	98.56% (0.03)	99.63% (0.01)
	k -MEANS	94.88%(0.09)	95.25%(0.14)	97.13%(0.14)	96.16%(0.04)	94.57%(0.11)	97.13%(0.14)
	DTW	59.76%(0.15)	54.02%(0.21)	69.52%(0.19)	56.97%(0.18)	64.98%(0.14)	85.20%(0.14)
	CASC	27.56%(0.10)	26.45%(0.12)	47.67%(0.14)	28.99%(0.14)	27.12%(0.10)	61.27%(0.11)
	SDP	37.85%(0.08)	31.39%(0.10)	51.27%(0.15)	39.36%(0.12)	37.31%(0.08)	62.97%(0.10)
	NAC	37.35%(0.08)	35.86%(0.11)	64.93%(0.14)	38.86%(0.12)	36.83%(0.08)	67.67%(0.12)
	SCORE	36.19%(0.11)	37.78%(0.15)	66.58%(0.17)	37.53%(0.14)	35.82%(0.11)	70.40%(0.13)
	GFL $_{d=3}$	98.91% (0.02)	99.29% (0.01)	99.69% (0.01)	99.11% (0.01)	98.73% (0.02)	99.69% (0.01)
210	k -MEANS	95.39%(0.09)	95.86%(0.14)	97.30%(0.14)	96.71%(0.03)	95.12%(0.11)	97.30%(0.14)
	DTW	79.11%(0.09)	80.64%(0.14)	91.46%(0.14)	80.22%(0.08)	79.08%(0.11)	91.83%(0.13)
	CASC	81.76%(0.09)	85.76%(0.13)	93.72%(0.13)	83.11%(0.06)	81.46%(0.11)	93.72%(0.13)
	SDP	39.17%(0.05)	35.18%(0.08)	60.02%(0.13)	40.51%(0.10)	38.87%(0.06)	64.43%(0.10)
	NAC	42.85%(0.06)	42.04%(0.10)	70.17%(0.14)	44.19%(0.10)	42.57%(0.07)	72.11%(0.12)
	SCORE	75.49%(0.09)	80.38%(0.13)	91.76%(0.13)	76.75%(0.07)	75.28%(0.10)	91.76%(0.13)

Scenario 2

This scenario moves to graphs on grids having four unbalanced regional clusters: top left \mathcal{C}_1 , top right \mathcal{C}_2 , bottom left \mathcal{C}_3 , and bottom right \mathcal{C}_4 . The nodal series use the same AR model in Scenario 1 and the same covariance parameters. To incorporate regional heterogeneity, cluster means were changed to $\mu_1 = -0.8$, $\mu_2 = 0.0$, $\mu_3 = 0.8$, and $\mu_4 = 1.6$.

We consider two graph sizes having $N = 144$ and $N = 196$ nodes. Both edge densities are sparser than Scenario 1. The unbalanced cluster sizes are 25, 30, 42, and 47 for $N = 144$ and 35, 40, 42, and 79 for $N = 196$. Figure 3 illustrates a simulated grid and its associated time series means. No clusters of nodes are visually distinguishable from the graph topology (without relying on nodal colors). Table 2 reports the sample means and standard deviations of the evaluation metrics across 50 simulations.

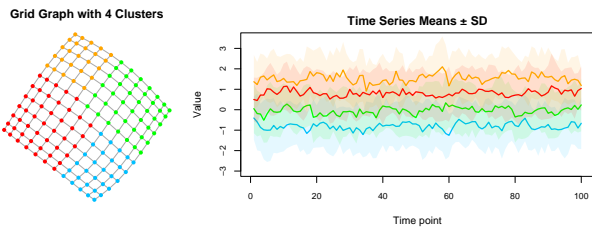


Figure 3. A simulated grid and its associated time series means. The left plot is a simulated graph with 144 nodes having unbalanced cluster sizes. The right plot shows the sample series means of the four clusters; one standard deviation bands are displayed.

Different from Scenario 1, the grid structure does not reveal cluster boundaries, making clustering based on the graph topology challenging. In this setting, cluster information resides in the nodal time series. The hybrid methods, CASC, SDP, and NAC, which rely on both adjacency matrix and nodal series perform poorly, suggesting that an uninformative spatial structure hinders spectral clustering even when

the time series exhibit cluster differences. Moreover, increasing the graph size N from 144 to 196 does not improve their performances, and can even degrade matters. Enlarging the grid jeopardizes graph-based approaches that emphasize structural cues. Interestingly, the SCORE method, which does not utilize any series for clustering, performs well when the correct number of clusters is supplied. The slight error here stems from the method’s tendency to produce four equal-sized squared regions, making some boundary nodes incorrectly assigned. In contrast, our GFL method continues to perform nicely, adapting to the absence of cluster signals in graph and relying on informative nodal series.

Table 2. Sample means (one standard deviation) of our evaluation metrics for Scenario 2. The best metric is in bold.

N	METHOD	NMI \uparrow	ARI \uparrow	ACC \uparrow	HOM \uparrow	COM \uparrow	PUR \uparrow
144	GFL $_{d=3}$	99.24% (0.01)	99.36% (0.01)	99.76% (0.01)	99.22% (0.02)	99.26% (0.01)	99.76% (0.01)
	k -MEANS	83.87%(0.10)	82.86%(0.16)	90.64%(0.17)	85.05%(0.08)	83.53%(0.11)	92.13%(0.14)
	DTW	58.34%(0.06)	46.60%(0.11)	65.82%(0.16)	58.37%(0.09)	59.29%(0.08)	75.89%(0.12)
	CASC	32.68%(0.03)	22.32%(0.04)	31.25%(0.06)	34.11%(0.10)	32.10%(0.02)	46.76%(0.06)
	SDP	28.92%(0.05)	18.43%(0.04)	36.50%(0.10)	30.30%(0.11)	28.37%(0.05)	50.26%(0.07)
	NAC	32.79%(0.09)	23.45%(0.09)	47.32%(0.12)	34.08%(0.13)	32.32%(0.09)	56.15%(0.10)
	SCORE	74.95%(0.05)	69.58%(0.10)	86.49%(0.12)	76.93%(0.03)	73.81%(0.07)	86.49%(0.12)
	GFL $_{d=3}$	99.71% (0.01)	99.75% (0.01)	99.92% (0.01)	99.71% (0.01)	99.71% (0.01)	99.92% (0.01)
196	k -MEANS	85.48%(0.08)	86.10%(0.13)	93.52%(0.13)	86.98%(0.04)	84.87%(0.09)	93.52%(0.13)
	DTW	57.66%(0.07)	47.02%(0.12)	65.21%(0.17)	58.24%(0.09)	58.08%(0.08)	74.69%(0.12)
	CASC	28.53%(0.02)	20.30%(0.03)	28.91%(0.04)	30.29%(0.10)	27.70%(0.01)	44.85%(0.06)
	SDP	27.22%(0.09)	17.94%(0.07)	28.67%(0.07)	28.92%(0.13)	26.43%(0.08)	48.37%(0.08)
	NAC	30.42%(0.08)	21.43%(0.07)	40.19%(0.12)	32.08%(0.12)	29.67%(0.07)	53.61%(0.09)
	SCORE	66.17%(0.04)	55.89%(0.08)	80.54%(0.11)	68.79%(0.04)	64.50%(0.06)	80.54%(0.11)

Scenario 3

Scenario 3 extends the block graphs in Scenario 1 by including correlations within the series in the same cluster. Here, a VAR model of order one is applied to incorporate cluster-specific correlations. The N -dimensional time series $\{\mathbf{Y}_t\}_{t=1}^T$ are generated simultaneously over all nodes via

$$\mathbf{Y}_t = \boldsymbol{\beta} + \Phi(\mathbf{Y}_{t-1} - \boldsymbol{\beta}) + \boldsymbol{\xi}_t, \quad t = 2, \dots, T$$

where $\boldsymbol{\beta} = (\beta_1, \beta_2, \dots, \beta_N)^\top$ is the nodal mean vector with $\beta_i = \mu_k$ for $i \in \mathcal{C}_k$. The error $\boldsymbol{\xi}_t$ is sampled as $\mathcal{N}(\mathbf{0}_N, \boldsymbol{\Sigma})$ for each t , where $\boldsymbol{\Sigma} = \{\Sigma_{i,j}\}_{i,j=1,\dots,N}$ has the intra-cluster correlations $\Sigma_{i,j} = 1 \forall i = j$, $\Sigma_{i,j} = \rho \forall i \neq j$, and $i, j \in \mathcal{C}_k$, $k \in \{1, 2, 3\}$, and $\Sigma_{i,j} = 0$ otherwise. We take $\rho = 0.3$, which induces moderate correlation.

The VAR coefficient is taken as $\Phi = 0.5\mathbf{I}_N$ and the means for the three clusters are repeated from Scenario 1. Series from different clusters are statistically independent. Our simulations start with $\mathbf{Y}_1 = \mathbf{0}$ and burn-in is used for 100 iterations to ensure stationary nodal series. Figure 4 shows a simulated block graph and the associated series sample means. Comparing to Scenario 1, the series means are not as well separated, making clustering more difficult.

Table 3 reports the means and standard deviations of our evaluation metrics over 50 simulations. With 120 nodes, k -means and CASC methods again provide good clusterings. CASC, which leverages nodal covariates via pair-wise similarity, benefits from the positive intra-cluster correlations. When the number of nodes increases to 210, competitors improve significantly (more than in Scenario 1), exploiting

the temporal correlation between nodes to improve performance. Our GFL method slightly degrades from Scenario 1, but still maintains accuracy and is often the best method. Even in the presence of modest intra-nodal correlation, our GFL clustering method continues to perform well.

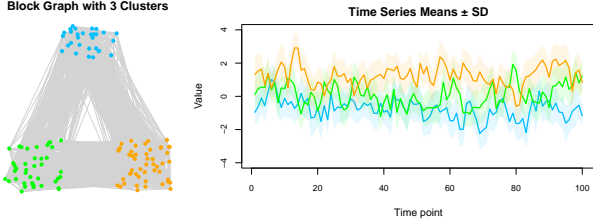


Figure 4. A simulated graph and nodal time series means. The left plot shows a simulated graph with unbalanced cluster sizes and 120 nodes. The right plot shows the sample series means of the three clusters; one standard deviation bands are again displayed.

Table 3. Sample means (one standard deviation) of our evaluation metrics for Scenario 3. The best metric is in bold.

N	METHOD	NMI \uparrow	ARI \uparrow	ACC \uparrow	HOM \uparrow	COM \uparrow	PUR \uparrow
120	GFL- $d=3$	98.62%(0.05)	98.36% (0.07)	98.88% (0.05)	98.03%(0.07)	99.55% (0.01)	98.88% (0.01)
	k -MEANS	98.73% (0.08)	98.00%(0.14)	98.05%(0.14)	100.0% (0.00)	99.45%(0.11)	98.05%(0.14)
	DTW	70.09%(0.20)	65.29%(0.26)	77.87%(0.21)	68.23%(0.22)	74.12%(0.19)	87.87%(0.15)
	CASC	98.73% (0.09)	98.00%(0.14)	98.05%(0.14)	100.0% (0.00)	98.45%(0.11)	98.05%(0.14)
	SDP	90.44%(0.17)	85.92%(0.26)	87.37%(0.24)	91.08%(0.17)	90.84%(0.17)	93.67%(0.15)
	NAC	81.64%(0.09)	84.97%(0.13)	93.43%(0.13)	83.16%(0.06)	81.10%(0.10)	93.43%(0.13)
	SCORE	39.08%(0.12)	39.98%(0.15)	69.05%(0.16)	40.47%(0.15)	38.67%(0.13)	71.83%(0.13)
210	GFL- $d=3$	98.40%(0.06)	97.66%(0.09)	98.26% (0.07)	97.51%(0.09)	99.87% (0.01)	99.97% (0.01)
	k -MEANS	98.68% (0.09)	98.00% (0.14)	98.03%(0.14)	100.0% (0.00)	98.41%(0.11)	98.03%(0.14)
	DTW	89.86%(0.10)	90.96%(0.14)	95.59%(0.14)	91.13%(0.06)	89.64%(0.11)	95.59%(0.14)
	CASC	98.63%(0.09)	97.97%(0.14)	98.02%(0.14)	99.95%(0.01)	98.36%(0.11)	98.02%(0.14)
	SDP	97.42%(0.12)	96.60%(0.16)	96.94%(0.15)	98.69%(0.08)	97.21%(0.13)	97.50%(0.14)
	NAC	93.04%(0.09)	94.32%(0.14)	96.77%(0.14)	94.40%(0.03)	92.73%(0.11)	96.77%(0.14)
	SCORE	74.11%(0.09)	79.05%(0.13)	91.28%(0.13)	75.44%(0.07)	73.83%(0.10)	91.28%(0.13)

5.2. California County Temperatures

We now cluster counties in the state of California via observed temperatures. California contains both the highest and lowest elevations in the contiguous United States. Its coastal proximity to the Pacific Ocean, neighboring desert environments, and broad latitudinal span lead to significant temperature heterogeneity, making clustering counties in California an interesting yet challenging problem. There are $N = 58$ counties in the state, all of which report data. Monthly average temperatures over the 14-year period January 2011 - December 2024 are studied. The data come from the National Centers for Environmental Information. Recent clusterings (by station, not county) of California climate appear in (Abatzoglou et al., 2009). While we examine the 14-year record to mitigate the impact of non-stationarity on results, California climate trend studies appear in (LaDochy et al., 2007) and (Walton & Hall, 2018).

A network with 58 nodes representing all counties was generated; two counties are connected by an edge if they share common border. The goal here is to utilize both spatial proximity of the counties and their temperature series to identify useful climate regions within the state. Some pre-processing was implemented to obtain stationary series. Specifically, with $\{Y_t\}_{t=1}^n$ denoting a county monthly series, we convert

to a standardized measurement by examining

$$S_{kT+\nu} := \frac{Y_{kT+\nu} - \hat{\mu}_\nu}{\hat{\sigma}_\nu},$$

where $k \in \{0, 1, \dots, n_{\text{yr}} - 1\}$ and $\nu \in \{1, 2, \dots, T\}$ is the calendar month of the year. Here, $n_{\text{yr}} = 14$ and $T = 12$ is the number of calendar months. Estimates of the month ν mean μ_ν and its standard deviation σ_ν are

$$\hat{\mu}_\nu = \frac{1}{n_{\text{yr}}} \sum_{k=0}^{n_{\text{yr}}-1} Y_{kT+\nu}, \quad \hat{\sigma}_\nu^2 = \frac{\sum_{k=0}^{n_{\text{yr}}-1} (Y_{kT+\nu} - \hat{\mu}_\nu)^2}{n_{\text{yr}} - 1}.$$

This standardization removes the monthly mean and variance seasonality of temperatures, but preserves county-level variability. In this analysis, the latent dimension d is taken as three. Sensitivity analyses from the simulation study, provided in the Appendix, suggest that this choice is adequate. Figure 5 displays the results from our methods. Ten clusters were selected by silhouette scores. Results from competitors are discussed in the Appendix.



Figure 5. California county clustering from GFL.

The separation between coastal and inland regions is apparent, and the latitudinal transition from north to south is also observed. Cluster 2 and Cluster 8 are dominated by mountainous areas, whereas Clusters 1, 3, 7, 9 are characterized by lower elevations. The Bay Area is further divided into a Delta region (Cluster 1) and coastal region (Cluster 10), indicating that the clustering method has captured intricate climatic heterogeneity within the area. Moreover, Fresno, Tulare, and Kern Counties are leading contributors to agricultural production in the United States, and they

are grouped in Cluster 5 at the southern area of the Central Valley, a basin that receives upstream river inflow with sufficient heat. Despite counties are administratively defined, the resulting clusters exhibit clear regional differentiation.

In summary, the clustering is sensible, placing Desert Southeast, Mid-Coastal, Lower Coastal, Bay Area, San Joaquin Valley, Sierra Nevada Mountain, Coastal Northwest, and Mountainous Northeast counties into distinct regions. While the clustering is based on temperature dynamics, the resulting regions reveal underlying geographic and agricultural characteristics, with potential implications for resource allocation and policy planning.

5.3. Word Co-occurrence Network

We also analyze word usage from the novel David Copperfield, written by Charles Dickens in 1850. (Newman, 2006) constructed a word co-occurrence network containing 112 common adjectives and nouns from the book. The network nodes correspond to different words, and an undirected edge between two words indicates whether they occur adjacent to one another at a sentence within the novel.

Building on this network, we extend the data by constructing temporal trajectories for each word as a time series. Specifically, as the novel has 64 chapters, the novel is divided into $n = 64$ equally spaced segments. For each segment, we record the frequency of each word, yielding a sequence $C_i = (C_{1,i}, \dots, C_{n,i})^T$ that tracks usage of the i th word. To account for large differences in frequency usages of different words, we standardize each sequence via

$$Y_{t,i} = \frac{C_{t,i} - \bar{C}_i}{\hat{\sigma}_i}, \quad t = 1, \dots, n, \quad i \in \mathcal{V}_{\text{word}},$$

where \bar{C}_i and $\hat{\sigma}_i$ denote the respective sample mean and standard deviation of the word’s series. This standardization ensures that the analysis focuses on the relative temporal dynamics of word usage rather than count magnitudes.

Figure 6 displays our clustering. Node shapes indicate the true linguistic labels (noun or adjective), while colors depict estimated clusters. The results demonstrate that most nouns (●) fall in a cluster (Cluster 1) and most adjectives (■) into another (Cluster 2). The other two clusters are small, each containing no more than three words and connected only to a single node in the remaining network. Similar to (Newman & Leicht, 2007), our method recovers the bipartite structure without being explicitly prompted. In particular, Cluster 3 contains two words “*aunt*” and “*family*”, reflecting the prominence of family as a central theme in the novel and the pivotal role of Aunt Betsey. Unlike David’s mother, whose influence fades with her early passing, Aunt Betsey becomes the loving guardian, shaping David’s values and providing unwavering support throughout his growth.

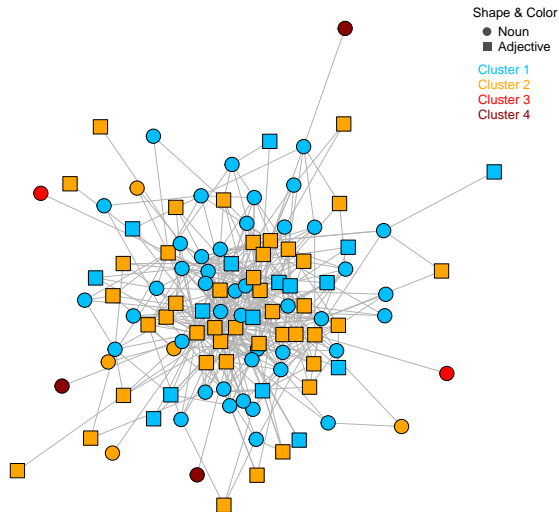


Figure 6. Word clustering from GFL. Node shapes indicate whether a word is an adjective or noun, while colors depict cluster members.

6. Discussion

This manuscript presents a decoder-only latent space model for clustering nodes in networks with node-level observed time series. By combining node-specific Gaussian priors, graph-fused LASSO regularization, and a neural network decoder, graph structures and attribute dynamics are integrated into low-dimensional representations that facilitate clustering. Simulations and applications to California county temperatures and word co-occurrence network produce good clustering performance.

Avenues for future development are apparent. Foremost, the type of nodal data could change. Multiple series, functional data, or multivariate attributes are feasible. The likelihood would need modification to accommodate such scenarios. The assumption of independent attributes across nodes could also be relaxed. On the network front, dyadic relations often have a degree of strength, perhaps continuous values in lieu of zero-one connections (Krivitsky, 2012; Wilson et al., 2017). Adapting our LASSO regularization to handle such weights would further improve clustering. Time-varying network edges can also arise (Malinovskaya et al., 2023). Methods to accommodate both nodal and dyadic attributes over time would extend applicability of our methods.

References

- Abatzoglou, J. T., Redmond, K. T., and Edwards, L. M. Classification of regional climate variability in the state of California. *Journal of Applied Meteorology and Climatology*, 48(8):1527–1541, 2009.
- Abbe, E. Community detection and stochastic block models: recent developments. *Journal of Machine Learning Research*, 18(177):1–86, 2018.
- Alaíz, C. M., Barbero, A., and Dorronsoro, J. R. Group fused LASSO. In *International Conference on Artificial Neural Networks*, pp. 66–73. Springer, 2013.
- Binkiewicz, N., Vogelstein, J. T., and Rohe, K. Covariate-assisted spectral clustering. *Biometrika*, 104(2):361–377, 2017.
- Boyd, S., Parikh, N., Chu, E., Peleato, B., Eckstein, J., et al. Distributed optimization and statistical learning via the alternating direction method of multipliers. *Foundations and Trends® in Machine Learning*, 3(1):1–122, 2011.
- Chen, Y., Jewell, S., and Witten, D. More powerful selective inference for the graph fused LASSO. *Journal of Computational and Graphical Statistics*, 32(2):577–587, 2023.
- Du, Y. and Mordatch, I. Implicit generation and modeling with energy based models. *Advances in Neural Information Processing Systems*, 32:3608 – 3618, 2019.
- Emmons, S., Kobourov, S., Gallant, M., and Börner, K. Analysis of network clustering algorithms and cluster quality metrics at scale. *PLoS One*, 11(7):e0159161, 2016.
- Hallac, D., Leskovec, J., and Boyd, S. Network LASSO: Clustering and optimization in large graphs. In *Proceedings of the 21th ACM SIGKDD International Conference on Knowledge Discovery and Data Mining*, pp. 387–396, 2015.
- Handcock, M. S., Raftery, A. E., and Tantrum, J. M. Model-based clustering for social networks. *Journal of the Royal Statistical Society Series A: Statistics in Society*, 170(2): 301–354, 2007.
- Hornik, K. Approximation capabilities of multilayer feedforward networks. *Neural Networks*, 4(2):251–257, 1991.
- Hornik, K., Stinchcombe, M., and White, H. Multilayer feedforward networks are universal approximators. *Neural Networks*, 2(5):359–366, 1989.
- Hu, Y. and Wang, W. Network-adjusted covariates for community detection. *Biometrika*, 111(4):1221–1240, 2024.
- Jackson, M. O. and Pernoud, A. Systemic risk in financial networks: A survey. *Annual Review of Economics*, 13(1):171–202, 2021.
- Jin, J. Fast community detection by SCORE. *Annals of Statistics*, 43(1):57–89, 2015. doi: 10.1214/14-AOS1265.
- Kingma, D. P. and Welling, M. Auto-encoding variational Bayes. *International Conference on Learning Representations*, 2014.
- Kipf, T. N. and Welling, M. Variational graph auto-encoders. *arXiv preprint arXiv:1611.07308*, 2016.
- Krivitsky, P. N. Exponential-family random graph models for valued networks. *Electronic Journal of Statistics*, 6: 1100–1128, 2012.
- LaDochy, S., Medina, R., and Patzert, W. Recent California climate variability: spatial and temporal patterns in temperature trends. *Climate Research*, 33(2):159–169, 2007.
- Macgregor, P. Fast and simple spectral clustering in theory and practice. *Advances in Neural Information Processing Systems*, 36:34410–34425, 2023.
- Madrid Padilla, O. H. and Chen, Y. Graphon estimation via nearest-neighbour algorithm and two-dimensional fused-LASSO denoising. *Canadian Journal of Statistics*, 51(1): 95–110, 2023.
- Malinovskaya, A., Killick, R., Leeming, K., and Otto, P. Statistical monitoring of european cross-border physical electricity flows using novel temporal edge network processes. *arXiv preprint arXiv:2312.16357*, 2023.
- Malliaros, F. D. and Vazirgiannis, M. Clustering and community detection in directed networks: A survey. *Physics Reports*, 533(4):95–142, 2013.
- Mattei, P.-A. and Frellsen, J. Leveraging the exact likelihood of deep latent variable models. *Advances in Neural Information Processing Systems*, 31, 2018.
- Newman, M. E. Finding community structure in networks using the eigenvectors of matrices. *Physical Review E—Statistical, Nonlinear, and Soft Matter Physics*, 74(3):036104, 2006.
- Newman, M. E. and Leicht, E. A. Mixture models and exploratory analysis in networks. *Proceedings of the National Academy of Sciences*, 104(23):9564–9569, 2007.
- Nijkamp, E., Hill, M., Han, T., Zhu, S.-C., and Wu, Y. N. On the anatomy of MCMC-based maximum likelihood learning of energy-based models. In *Proceedings of the*

- AAAI Conference on Artificial Intelligence, volume 34, pp. 5272–5280, 2020.
- Purohit, V., Repasky, M., Lu, J., Qiu, Q., Xie, Y., and Cheng, X. Posterior sampling via langevin dynamics based on generative priors. arXiv preprint arXiv:2410.02078, 2024.
- Sakoe, H. and Chiba, S. Dynamic programming algorithm optimization for spoken word recognition. IEEE Transactions on Acoustics, Speech, and Signal Processing, 26(1):43–49, 2003.
- Sewell, D. K. and Chen, Y. Latent space models for dynamic networks. Journal of the American Statistical Association, 110(512):1646–1657, 2015.
- Shai, S., Stanley, N., Granell, C., Taylor, D., and Mucha, P. J. Case studies in network community detection. In The Oxford Handbook of Social Networks. Oxford University Press, 2021. ISBN 9780190251765. doi:10.1093/oxfordhb/9780190251765.013.16.
- Shen, L., Amini, A., Josephs, N., and Lin, L. Bayesian community detection for networks with covariates. Bayesian Analysis, 1(1):1–28, 2024.
- Snijders, T. A. Statistical models for social networks. Annual Review of Sociology, 37(1):131–153, 2011.
- Su, X., Xue, S., Liu, F., Wu, J., Yang, J., Zhou, C., Hu, W., Paris, C., Nepal, S., Jin, D., et al. A comprehensive survey on community detection with deep learning. IEEE Transactions on Neural Networks and Learning Systems, 35(4):4682–4702, 2022.
- Vert, J.-P. and Bleakley, K. Fast detection of multiple change-points shared by many signals using group lars. Advances in Neural Information Processing Systems, 23, 2010.
- Walton, D. and Hall, A. An assessment of high-resolution gridded temperature datasets over california. Journal of Climate, 31(10):3789–3810, 2018.
- Wang, S., Paul, S., and De Boeck, P. Joint latent space model for social networks with multivariate attributes. Psychometrika, 88(4):1197–1227, 2023.
- Wang, Y., Yin, W., and Zeng, J. Global convergence of admm in nonconvex nonsmooth optimization. Journal of Scientific Computing, 78(1):29–63, 2019.
- Wang, Y.-X., Sharpnack, J., Smola, A. J., and Tibshirani, R. J. Trend filtering on graphs. Journal of Machine Learning Research, 17(105):1–41, 2016.
- Wilson, J. D., Denny, M. J., Bhamidi, S., Cranmer, S. J., and Desmarais, B. A. Stochastic weighted graphs: Flexible model specification and simulation. Social Networks, 49:37–47, 2017.
- Yan, B. and Sarkar, P. Covariate regularized community detection in sparse graphs. Journal of the American Statistical Association, 116(534):734–745, 2021.
- Yang, S. E., Wilson, J. D., Lu, Z.-L., and Cranmer, S. Functional connectivity signatures of political ideology. PNAS nexus, 1(3):pgac066, 2022.
- Yarotsky, D. Error bounds for approximations with deep ReLU networks. Neural Networks, 94:103–114, 2017.
- Yu, F., Yang, A. Y., and Zhang, T. A graph decomposition-based approach for the graph-fused LASSO. Journal of Statistical Planning and Inference, 235:106221, 2025.
- Yuan, M. and Lin, Y. Model selection and estimation in regression with grouped variables. Journal of the Royal Statistical Society Series B: Statistical Methodology, 68(1):49–67, 2006.
- Zhu, X., Caliskan, C., Christenson, D. P., Spiliopoulos, K., Walker, D., and Kolaczyk, E. D. Disentangling positive and negative partisanship in social media interactions using a coevolving latent space network with attractors model. Journal of the Royal Statistical Society Series A: Statistics in Society, 186(3):463–480, 2023.

A. Parameter Learning

A.1. Updating μ and ϕ

In this section, we derive the updates for prior parameter μ and decoder parameter ϕ . Denote the collection of parameters $\{\phi, \mu\}$ as θ . We first calculate the gradient of the log-likelihood $L(\theta)$ with respect to θ :

$$\begin{aligned}
 \nabla_{\theta} L(\theta) &= \nabla_{\theta} \sum_{i \in \mathcal{V}} \ln(P(\mathbf{Y}_i)) \\
 &= \sum_{i \in \mathcal{V}} \frac{1}{P(\mathbf{Y}_i)} \nabla_{\theta} P(\mathbf{Y}_i) \\
 &= \sum_{i \in \mathcal{V}} \frac{1}{P(\mathbf{Y}_i)} \nabla_{\theta} \int P(\mathbf{Y}_i, \mathbf{Z}_i) d\mathbf{Z}_i \\
 &= \sum_{i \in \mathcal{V}} \frac{1}{P(\mathbf{Y}_i)} \int \nabla_{\theta} P(\mathbf{Y}_i, \mathbf{Z}_i) d\mathbf{Z}_i \\
 &= \sum_{i \in \mathcal{V}} \frac{1}{P(\mathbf{Y}_i)} \int \left[P(\mathbf{Y}_i, \mathbf{Z}_i) \frac{1}{P(\mathbf{Y}_i, \mathbf{Z}_i)} \right] \left[\nabla_{\theta} P(\mathbf{Y}_i, \mathbf{Z}_i) \right] d\mathbf{Z}_i \\
 &= \sum_{i \in \mathcal{V}} \frac{1}{P(\mathbf{Y}_i)} \int P(\mathbf{Y}_i, \mathbf{Z}_i) \left[\nabla_{\theta} \ln(P(\mathbf{Y}_i, \mathbf{Z}_i)) \right] d\mathbf{Z}_i \\
 &= \sum_{i \in \mathcal{V}} \int \frac{P(\mathbf{Y}_i, \mathbf{Z}_i)}{P(\mathbf{Y}_i)} \left[\nabla_{\theta} \ln(P(\mathbf{Y}_i, \mathbf{Z}_i)) \right] d\mathbf{Z}_i \\
 &= \sum_{i \in \mathcal{V}} \int P(\mathbf{Z}_i | \mathbf{Y}_i) \left[\nabla_{\theta} \ln(P(\mathbf{Y}_i, \mathbf{Z}_i)) \right] d\mathbf{Z}_i \\
 &= \sum_{i \in \mathcal{V}} \mathbb{E} \left(\nabla_{\theta} \ln(P(\mathbf{Y}_i | \mathbf{Z}_i) P(\mathbf{Z}_i)) \middle| \mathbf{Y}_i \right) \\
 &= \sum_{i \in \mathcal{V}} \mathbb{E} \left(\nabla_{\theta} \ln(P(\mathbf{Y}_i | \mathbf{Z}_i)) \middle| \mathbf{Y}_i \right) + \sum_{i \in \mathcal{V}} \mathbb{E} \left(\nabla_{\theta} \ln(P(\mathbf{Z}_i)) \middle| \mathbf{Y}_i \right).
 \end{aligned}$$

Note that the expectation in the gradient is now with respect to the posterior density function $P(\mathbf{Z}_i | \mathbf{Y}_i) \propto P(\mathbf{Y}_i | \mathbf{Z}_i) \times P(\mathbf{Z}_i)$. Furthermore, denote the objective function in (4) as

$$\mathcal{L}(\mu_i) = -L(\phi, \mu_i) + \frac{\gamma}{2} \sum_{j \in \mathcal{B}(i)} \|\mu_i - \mu_j - \nu_{i,j} + \mathbf{w}_{i,j}\|_2^2.$$

The gradient of $\mathcal{L}(\mu_i)$ with respect to the prior parameter $\mu_i \in \mathbb{R}^d$ at a specific node i is

$$\begin{aligned}
 \nabla_{\mu_i} \mathcal{L}(\mu_i) &= -\mathbb{E} \left(\nabla_{\mu_i} \ln(P(\mathbf{Z}_i)) \middle| \mathbf{Y}_i \right) + \gamma \sum_{j \in \mathcal{B}(i)} (\mu_i - \mu_j - \nu_{i,j} + \mathbf{w}_{i,j}) \\
 &= -\mathbb{E}(\mathbf{Z}_i - \mu_i | \mathbf{Y}_i) + \gamma |\mathcal{B}(i)| \mu_i + \gamma \sum_{j \in \mathcal{B}(i)} (-\mu_j - \nu_{i,j} + \mathbf{w}_{i,j}) \\
 &= -\mathbb{E}(\mathbf{Z}_i | \mathbf{Y}_i) + (1 + \gamma |\mathcal{B}(i)|) \mu_i + \gamma \sum_{j \in \mathcal{B}(i)} (-\mu_j - \nu_{i,j} + \mathbf{w}_{i,j}).
 \end{aligned}$$

Setting the gradient $\nabla_{\mu_i} \mathcal{L}(\mu_i)$ to zeros and solve for μ_i , we have

$$\begin{aligned}
 \mathbf{0} &= -\mathbb{E}(\mathbf{Z}_i | \mathbf{Y}_i) + (1 + \gamma |\mathcal{B}(i)|) \mu_i + \gamma \sum_{j \in \mathcal{B}(i)} (-\mu_j - \nu_{i,j} + \mathbf{w}_{i,j}) \\
 (1 + \gamma |\mathcal{B}(i)|) \mu_i &= \mathbb{E}(\mathbf{Z}_i | \mathbf{Y}_i) - \gamma \sum_{j \in \mathcal{B}(i)} (-\mu_j - \nu_{i,j} + \mathbf{w}_{i,j}) \\
 \mu_i &= (1 + \gamma |\mathcal{B}(i)|)^{-1} \left[\mathbb{E}(\mathbf{Z}_i | \mathbf{Y}_i) + \gamma \sum_{j \in \mathcal{B}(i)} (\mu_j + \nu_{i,j} - \mathbf{w}_{i,j}) \right].
 \end{aligned}$$

Similarly, the gradient of $\mathcal{L}(\phi, \mu) = -L(\phi, \mu)$ with respect to the decoder parameter ϕ is

$$\nabla_{\phi} \mathcal{L}(\phi, \mu) = - \sum_{i \in \mathcal{V}} \mathbb{E} \left(\nabla_{\phi} \ln (P(\mathbf{Y}_i | \mathbf{Z}_i)) \middle| \mathbf{Y}_i \right).$$

A.2. Updating ν

In this section, we present the derivation to update $\nu_{i,j}$ for $(i, j) \in \mathcal{E}$, which is equivalent to solving a Group LASSO problem. Denote the objective function in (5) as $\mathcal{L}(\nu_{i,j})$. When $\nu_{i,j} \neq \mathbf{0}$, the gradient of $\mathcal{L}(\nu_{i,j})$ with respect to $\nu_{i,j}$ is

$$\nabla_{\nu_{i,j}} \mathcal{L}(\nu_{i,j}) = \lambda \frac{\nu_{i,j}}{\|\nu_{i,j}\|_2} - \gamma(\mu_i - \mu_j - \nu_{i,j} + \mathbf{w}_{i,j}).$$

Setting the gradient to zeros, we have

$$\begin{aligned} \mathbf{0} &= \frac{\lambda}{\|\nu_{i,j}\|_2} \nu_{i,j} + \gamma \cdot \nu_{i,j} - \gamma(\mu_i - \mu_j + \mathbf{w}_{i,j}) \\ \nu_{i,j} &= \left(\frac{\lambda}{\|\nu_{i,j}\|_2} + \gamma \right)^{-1} \left[\gamma(\mu_i - \mu_j + \mathbf{w}_{i,j}) \right] \end{aligned} \quad (11)$$

which involves $\nu_{i,j}$ on both sides. Calculating the Euclidean norm of (11) on both sides and rearrange the terms, we have

$$\begin{aligned} \|\nu_{i,j}\|_2 &= \left(\frac{\lambda + \gamma \|\nu_{i,j}\|_2}{\|\nu_{i,j}\|_2} \right)^{-1} \|\gamma(\mu_i - \mu_j + \mathbf{w}_{i,j})\|_2 \\ \lambda + \gamma \|\nu_{i,j}\|_2 &= \|\gamma(\mu_i - \mu_j + \mathbf{w}_{i,j})\|_2 \\ \|\nu_{i,j}\|_2 &= \|\mu_i - \mu_j + \mathbf{w}_{i,j}\|_2 - \frac{\lambda}{\gamma}. \end{aligned}$$

Plugging the result of $\|\nu_{i,j}\|_2$ back into (11), the solution of $\nu_{i,j}$ is

$$\begin{aligned} \nu_{i,j} &= \left(\frac{\lambda + \gamma \|\mu_i - \mu_j + \mathbf{w}_{i,j}\|_2 - \lambda}{\|\mu_i - \mu_j + \mathbf{w}_{i,j}\|_2 - \frac{\lambda}{\gamma}} \right)^{-1} \left[\gamma(\mu_i - \mu_j + \mathbf{w}_{i,j}) \right] \\ &= \left(\frac{\|\mu_i - \mu_j + \mathbf{w}_{i,j}\|_2 - \frac{\lambda}{\gamma}}{\gamma \|\mu_i - \mu_j + \mathbf{w}_{i,j}\|_2} \right) \left[\gamma(\mu_i - \mu_j + \mathbf{w}_{i,j}) \right] \\ &= \left(1 - \frac{\lambda}{\gamma \|\mu_i - \mu_j + \mathbf{w}_{i,j}\|_2} \right) (\mu_i - \mu_j + \mathbf{w}_{i,j}). \end{aligned}$$

Furthermore, when $\nu_{i,j} = \mathbf{0}$, a subgradient vector \mathbf{b} of $\|\nu_{i,j}\|_2$ needs to satisfy that $\|\mathbf{b}\|_2 \leq 1$. Since

$$\begin{aligned} \mathbf{0} &\in \lambda \mathbf{b} - \gamma(\mu_i - \mu_j + \mathbf{w}_{i,j}), \\ \lambda \mathbf{b} &\in \gamma(\mu_i - \mu_j + \mathbf{w}_{i,j}), \end{aligned}$$

we obtain the condition that $\nu_{i,j}$ becomes zeros when $\gamma \|\mu_i - \mu_j + \mathbf{w}_{i,j}\|_2 \leq \lambda$. Therefore, we can update $\nu_{i,j}$ for $(i, j) \in \mathcal{E}$ with the following equation:

$$\nu_{i,j} = \left(1 - \frac{\lambda}{\gamma \|\mathbf{s}_{i,j}\|_2} \right)_+ \mathbf{s}_{i,j}$$

where $\mathbf{s}_{i,j} = \mu_i - \mu_j + \mathbf{w}_{i,j}$ and $(\cdot)_+ = \max(0, \cdot)$.

A.3. Neural Decoder

For flexibility of decoder $P_{\phi}(\mathbf{Y}_i | \mathbf{Z}_i)$, the mean $\mathbf{h}_{\phi}(\cdot)$ is parameterized by a three-layer ReLU neural network. Specifically, $\mathbf{h}_{\phi}(\cdot)$ is taken as a three-layer rectified linear unit (ReLU) neural network:

$$\mathbf{h}_{\phi}(\mathbf{Z}_i) = \mathbf{W}_3 \text{ReLU}(\mathbf{W}_2 \text{ReLU}(\mathbf{W}_1 \mathbf{Z}_i + \mathbf{b}_1) + \mathbf{b}_2) + \mathbf{b}_3,$$

where $\mathbf{W}_1 \in \mathbb{R}^{h_1 \times d}$, $\mathbf{W}_2 \in \mathbb{R}^{h_2 \times h_1}$, and $\mathbf{W}_3 \in \mathbb{R}^{n \times h_2}$ are weights and $\mathbf{b}_1 \in \mathbb{R}^{h_1 \times 1}$, $\mathbf{b}_2 \in \mathbb{R}^{h_2 \times 1}$, and $\mathbf{b}_3 \in \mathbb{R}^{n \times 1}$ are bias parameters. Here, $\text{ReLU}(x) = \max(0, x)$ is the element-wise ReLU activation function at x , and model parameters are collected into ϕ .

Table 4 summarizes the number of model parameters and data points, when the node size is $|\mathcal{V}| = 120$, the latent dimension is $d = 3$, and the sequence length is $n = 100$. The neural network decoder consists of two hidden layers, each containing 32 neurons. The three-layer ReLU neural networks can be expressive without being over-parameterized.

Table 4. Number of parameters and data points.

NOTATION	DESCRIPTION	QUANTITY
ϕ	NEURAL NETWORKS	$32 \times 3 + 32 \times 32 + 100 \times 32 + 32 \times 1 + 32 \times 1 + 100 \times 1 = 4,484$
$\{\mu_i\}_{i \in \mathcal{V}}$	PRIOR MEANS	$ \mathcal{V} \times 3 = 360$
$\{\mathbf{Y}_i\}_{i \in \mathcal{V}}$	NODAL SERIES	$ \mathcal{V} \times 100 = 12,000$
$\mathcal{G} = (\mathcal{V}, \mathcal{E})$	GRAPHICAL STRUCTURES	$ \mathcal{E} $

The negative log-likelihood that involves latent variable $\mathbf{Z}_i \in \mathbb{R}^d$ and observed series $\mathbf{Y}_i \in \mathbb{R}^n$ is lower bounded by

$$\begin{aligned}
 -\ln(P(\mathbf{Y}_i)) &= -\ln \left[\int \frac{1}{(2\pi)^{n/2}} \exp\left(-\frac{1}{2}\|\mathbf{Y}_i - \mathbf{h}_\phi(\mathbf{Z}_i)\|_2^2\right) \cdot \frac{1}{(2\pi)^{d/2}} \exp\left(-\frac{1}{2}\|\mathbf{Z}_i - \mu_i\|_2^2\right) d\mathbf{Z}_i \right] \\
 &\geq -\ln \left[\frac{1}{(2\pi)^{(n+d)/2}} \int \exp\left(-\frac{1}{2}\|\mathbf{Z}_i - \mu_i\|_2^2\right) d\mathbf{Z}_i \right] \\
 &\geq -\ln \left[\frac{1}{(2\pi)^{n/2}} \right] \\
 &\geq \frac{n}{2} \ln(2\pi)
 \end{aligned} \tag{12}$$

where (12) follows because $\exp(-\frac{1}{2}x^2) \leq 1$. While the likelihood function of some latent space models can be unbounded (Mattei & Frelsen, 2018), the minimization problem in (2) is valid and meaningful.

A.4. Computation Complexity

The algorithm to solve (3) via ADMM is presented in Algorithm 1. The computation complexity is at least of order $O(A(|\mathcal{V}|skd + B|\mathcal{V}|sn + |\mathcal{V}|sd + |\mathcal{E}|d))$; additional gradient computation for neural networks is required in sub-routines.

Elaborating, in each of A iterations of ADMM, Langevin dynamics generate s samples for each i , each requiring k MCMC steps (and has dimension of d). Next, the decoder parameters ϕ are updated via B iterations of the Adam optimizer across all nodes using the s generated samples. The output of neural networks has length n for each node. Then, the node-specific prior parameters μ_i are updated in closed form at each iteration using the MCMC samples, which incurs a computational cost that is linear in $|\mathcal{V}|sd$. Finally, the slack variables $\nu_{i,j}$ are updated, resulting in a complexity of $O(|\mathcal{E}|d)$. The scaled dual variables $w_{i,j}$ are updated in closed form with similar computation complexity.

In summary, the ADMM procedure decomposes a complex optimization problem into smaller components, targeting the smaller components individually. While our methods are computationally demanding, substantial clustering performance is gained, as demonstrated in the simulation study.

B. Additional Details of Experiments

B.1. Implementation Details

To simulate realistic network structures, block and grid graphs are considered. For the block graphs in Scenarios 1 and 3, the edge density is roughly $2|\mathcal{E}||\mathcal{V}|^{-2} \approx 0.4$. In Scenario 2, the edge density for a 12×12 grid is about $2|\mathcal{E}||\mathcal{V}|^{-2} \approx 0.051$, and the edge density for a 14×14 grid is about $2|\mathcal{E}||\mathcal{V}|^{-2} \approx 0.038$. In reality, many networks are considered small and sparse, and the objective of researchers is to draw insights from limited information.

For particulars of competitor methods, k -means constructs clusters by minimizing within-cluster squared distances. DTW

Algorithm 1 Latent space graph-fused LASSO

-
- 1: **Input:** learning iterations A, B, D , tuning parameter λ , penalty parameter γ , learning rate η , observed data $\{\mathbf{Y}_i\}_{i \in \mathcal{V}}$, initialization $\{\phi^{(1)}, \mu^{(1)}, \nu^{(1)}, \mathbf{w}^{(1)}\}$
 - 2: **for** $a = 1, \dots, A$ **do**
 - 3: **for** $i \in \mathcal{V}$ **do**
 - 4: draw samples $\mathbf{Z}_{1,i}, \dots, \mathbf{Z}_{s,i}$ from $P(\mathbf{Z}_i | \mathbf{Y}_i)$ according to (9)
 - 5: **end for**
 - 6: **for** $b = 1, \dots, B$ **do**
 - 7: $\phi_{(b+1)} = \text{Adam}(\phi_{(b)}, \nabla_{\phi} \mathcal{L}(\phi, \mu), \eta)$
 - 8: **end for**
 - 9: $\mu_i^{(a+1)} = (1 + \gamma |\mathcal{B}(i)|)^{-1} \left[s^{-1} \sum_{u=1}^s \mathbf{Z}_{u,i} + \gamma \sum_{j \in \mathcal{B}(i)} (\mu_j^{(a)} + \nu_{i,j}^{(a)} - \mathbf{w}_{i,j}^{(a)}) \right], \forall i \in \mathcal{V}$
 - 10: Let $\nu_{i,j}^{(a+1)}$ be updated according to (8) for $(i, j) \in \mathcal{E}$
 - 11: $\mathbf{w}_{i,j}^{(a+1)} = \mu_i^{(a+1)} - \mu_j^{(a+1)} - \nu_{i,j}^{(a+1)} + \mathbf{w}_{i,j}^{(a)}, \forall (i, j) \in \mathcal{E}$
 - 12: **end for**
 - 13: $\hat{\mu} \leftarrow \mu^{(a+1)}$
 - 14: **Output:** learned prior parameters $\hat{\mu}$
-

method measures similarities between time series by aligning them via a non-linear time warping. CASC method leverages the nodal covariate \mathbf{X} via $\mathbf{L}_{\tau} \mathbf{L}_{\tau} + \alpha \mathbf{X} \mathbf{X}^{\top}$ to improve spectral clustering performance; here, \mathbf{L}_{τ} is the regularized graph Laplacian. SDP method converts clustering issues into a convex semi-definite procedure, enabling efficient approximation of the optimal partition. Specifically, SDP maximizes the inner product between $\mathbf{A} + \lambda \mathbf{K}$ and a cluster label matrix; here, \mathbf{A} is an adjacency matrix and $\mathbf{K} \in \mathbb{R}_+^{N \times N}$ is a kernel matrix whose (i, j) th entry quantifies the similarity between covariates from nodes i and j . NAC method incorporates node covariates into spectral clustering through the network-adjusted covariate matrix $\mathbf{A} \mathbf{X} + \mathbf{D}_{\alpha} \mathbf{X} \in \mathbb{R}^{N \times p}$ with diagonal weight matrix \mathbf{D}_{α} and covariate matrix \mathbf{X} . The SCORE method identifies communities through the ratios between the first leading eigenvector and the other leading eigenvectors.

For competitors, the true number of clusters from the simulated data and their default configurations are used during implementation. For GFL, we run our experiments with A100 GPU. As the objective function in (3) is highly non-convex due to the neural networks and sub-routines requiring MCMC sampling, specifying standard convergence criteria is impractical. The algorithm is implemented for a preset number of iterations, as an early stopping strategies to avoid over-fitting, which is commonly used in machine learning.

B.2. Visualization

For both simulation and real data experiments, the choice of latent dimension $d = 3$ permits visualizations of learned prior parameters in latent space. Figure 7 illustrates the estimated $\hat{\mu} \in \mathbb{R}^{N \times 3}$ for a realization from Scenarios 1 - 3 with $d = 3$. We can see that the estimated prior parameters have captured meaningful boundary between clusters, enforced by graph-fused LASSO regularization.

Figure 8 displays the estimated $\hat{\mu} \in \mathbb{R}^{58 \times 3}$ from the California county temperature data analyzed in Section 5. From left to right, each panel displays a pairwise projection of the three latent dimensions. The first panel shows that counties within the same cluster are positioned closely in the latent space. The second and third panels of the graphic also show dome-shape relations for the third dimension (dim3) intersecting the first two dimensions (dim1 and dim2). Taken together, the three-dimensional latent space exhibits clear boundaries between clusters.

Figure 9 displays the estimated $\hat{\mu} \in \mathbb{R}^{112 \times 3}$ from the word co-occurrence network analyzed in Section 5. While the boundary between the blue and orange clusters are not visually apparent, the k -means algorithm and the silhouette score applied to the estimated prior parameters indicate the presence of two distinct clusters rather than a single one. In other words, partitioning the data points into two clusters results in more cohesive groupings with clearer separation. Overall, for the two real data experiments, the estimated prior parameters have captured meaningful separations between clusters in the latent space, driven by the graph-fused LASSO regularization.

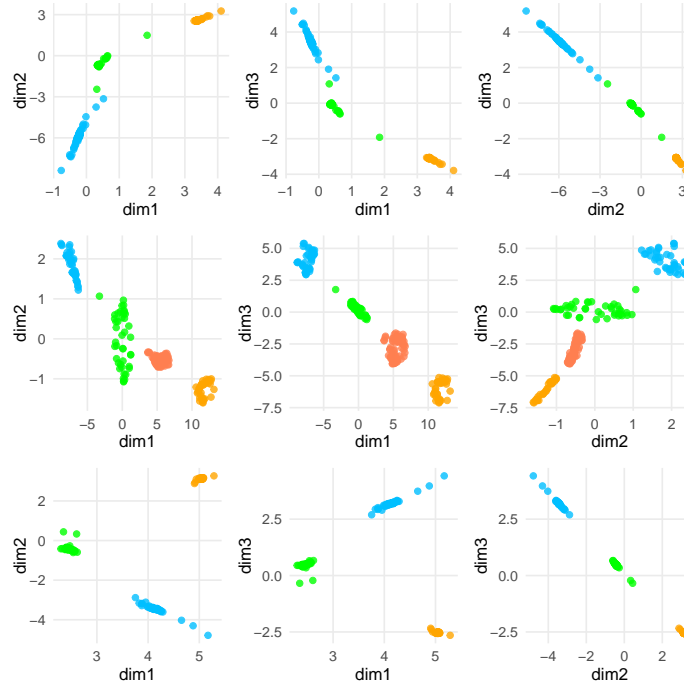


Figure 7. Illustration of estimated $\hat{\mu} \in \mathbb{R}^{N \times d}$ for a realization from Scenarios 1 - 3, where the latent dimension is $d = 3$. Each row, from top to bottom, corresponds to a scenario. Each column, from left to right, displays a pairwise projection of the three latent dimensions. The node colors depict the ground truth labels.

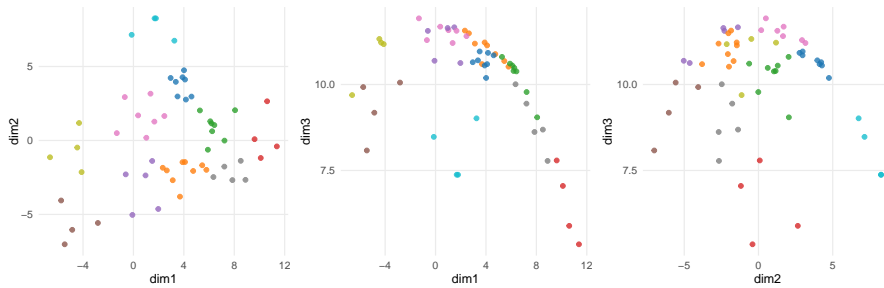


Figure 8. Visualization of estimated $\hat{\mu} \in \mathbb{R}^{58 \times 3}$. Each data point represents one of the 58 counties in California. Node colors represent the clusters detected by our method.

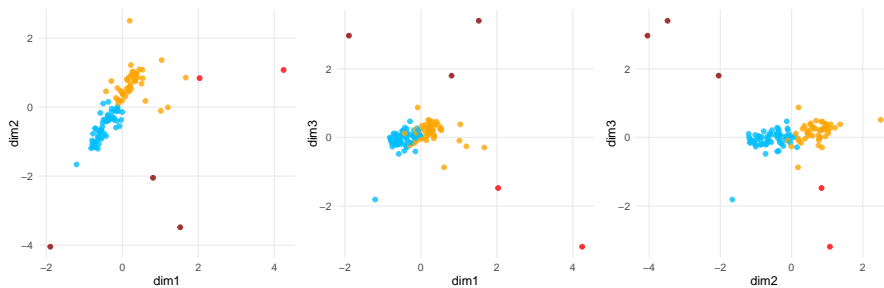


Figure 9. Visualization of estimated $\hat{\mu} \in \mathbb{R}^{112 \times 3}$. Each data point represents one of the 112 words. Node colors represent the clusters detected by our method.

B.3. Results from Competitors

Figure 10 displays the California county clusterings from the competitor methods. Ten clusters are selected to be comparable to our result; if the numbers of clusters for competitors are selected by silhouette scores, fewer clusters and unrealistic results arise. Overall, the clusterings are less geographically coherent. For the k -means, DTW, and SDP methods, Inyo County in the Owens Valley is grouped with the Desert South cluster. The DTW, CASC, and SCORE methods produce clusters that span both coastal and inland regions. For the NAC method, San Diego County and Orange County are placed in the Desert South cluster, while Kern County in the Central Valley is grouped with the Lower Coastal region. For the k -means and CASC methods, the Northeast Mountain counties mix with the Coastal Northwest counties. With understanding of local geography, these results are less plausible and difficult to justify.

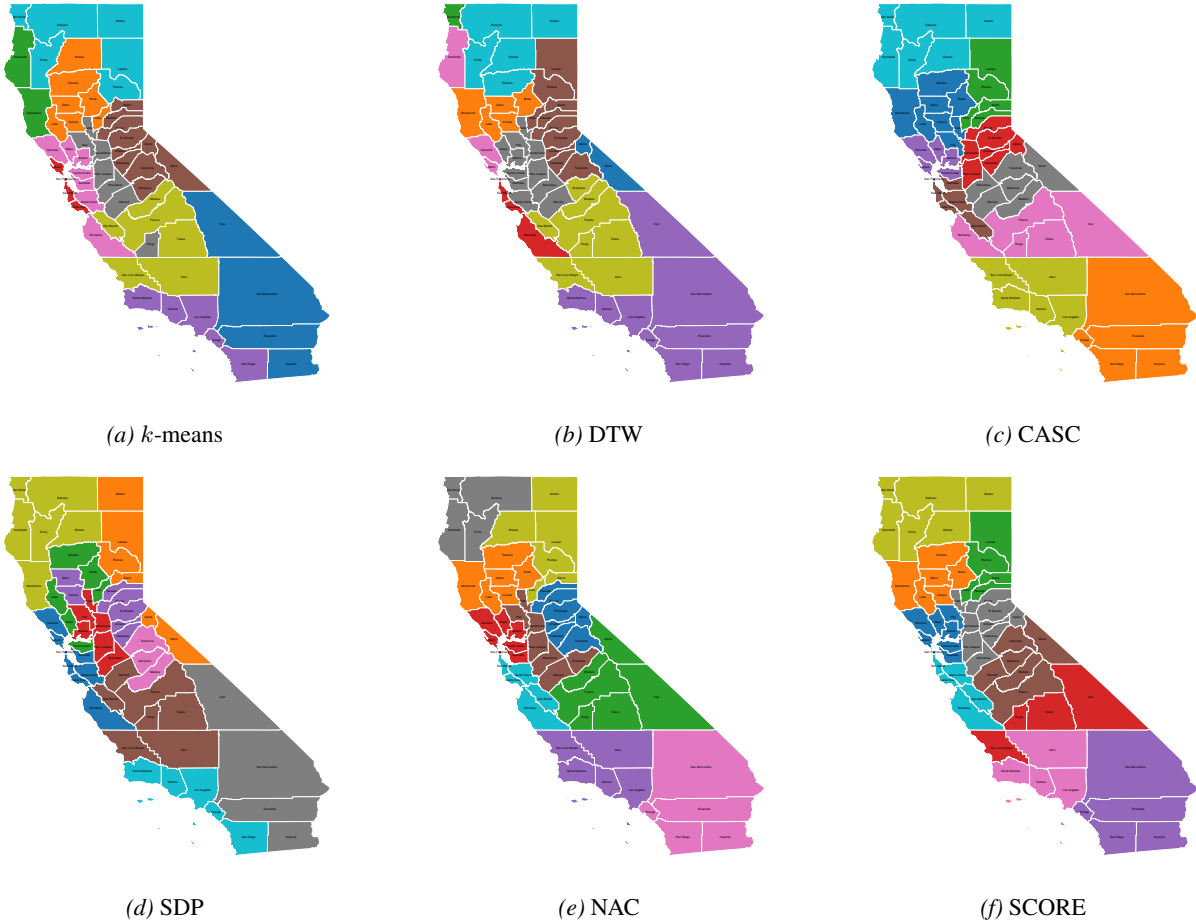


Figure 10. California county clustering from competitor methods with ten clusters.

Figure 11 displays the clusterings of the word co-occurrence network from competitors. Based on the linguistic nature (noun or adjective) of the words, two clusters were chosen. Most competitors fail to discover coherent clusters, resulting in substantial mixing of nouns and adjectives. The k -means and DTW methods disregard the co-occurrence structure delineated by the graph, and the SCORE method overlooks the narrative dynamics across chapters. The SDP and NAC methods may integrate both sources of information improperly to exhibit degraded clustering performance. In contrast, our method yields more linguistically coherent partitions.

B.4. Sensitivity Analysis

The three simulation studies in Scenarios 1 - 3 are repeated for the proposed GFL method, with varying latent dimensions $d \in \{3, 5, 7, 10\}$. Table 5 reports the results, with the values for $d = 3$ directly duplicated from Tables 1, 2, and 3 for comparison. The proposed method is robust when the latent dimension is relatively low. However, when $d = 10$, the

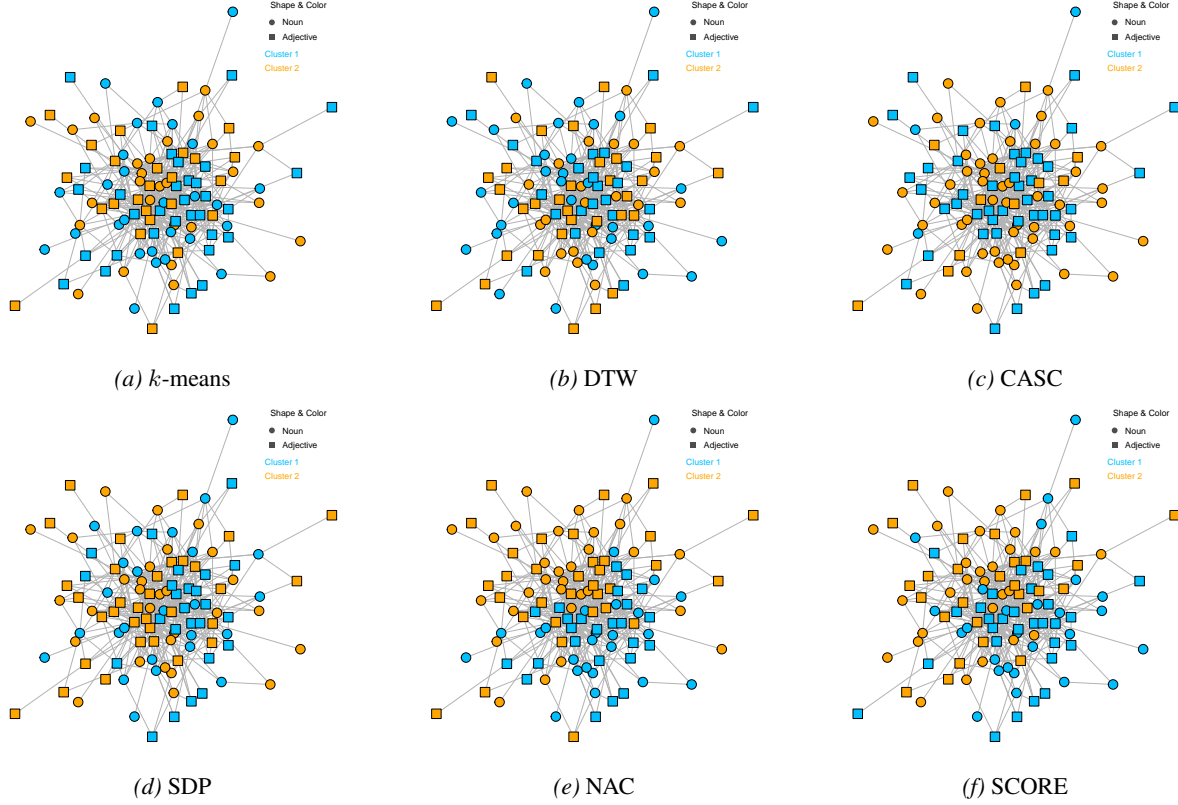


Figure 11. Word clustering from competitor methods. Node shapes indicate whether a word is an adjective or noun, while colors depict cluster members.

performance declines significantly, likely due to over-fitting. In this case, the latent representation, which contains both temporal and structural information, could include excessive noise that deteriorates the clustering results.

Table 5. Sample means (one standard deviation) of our evaluation metrics for varied latent dimension $d \in \{3, 5, 7, 10\}$ and Scenarios 1-3. The best metric is in bold.

SCENARIO, N	d	NMI \uparrow	ARI \uparrow	ACC \uparrow	HOM \uparrow	COM \uparrow	PUR \uparrow
S1, 120	3	98.52%(0.03)	98.96%(0.02)	99.63%(0.01)	98.49%(0.03)	98.56%(0.03)	99.63%(0.01)
	5	98.80% (0.02)	99.17% (0.02)	99.72% (0.01)	98.79% (0.02)	98.80% (0.02)	99.72% (0.01)
	7	98.39%(0.03)	98.82%(0.02)	99.38%(0.02)	98.63%(0.03)	98.19%(0.04)	99.38%(0.02)
	10	80.36%(0.10)	72.73%(0.13)	79.77%(0.10)	69.82%(0.15)	97.33%(0.05)	99.27%(0.02)
S1, 210	3	98.91%(0.02)	99.29%(0.01)	99.69%(0.01)	99.11%(0.01)	98.73%(0.02)	99.69%(0.01)
	5	99.40% (0.01)	99.62% (0.01)	99.88% (0.01)	99.40% (0.01)	99.40% (0.01)	99.88% (0.01)
	7	98.74%(0.02)	99.20%(0.01)	99.70%(0.01)	98.83%(0.01)	98.66%(0.02)	99.70%(0.01)
	10	83.01%(0.10)	75.00%(0.17)	81.23%(0.13)	74.16%(0.18)	97.96%(0.03)	99.51%(0.01)
S2, 144	3	99.24%(0.01)	99.36%(0.01)	99.76% (0.01)	99.22%(0.02)	99.26% (0.01)	99.76% (0.01)
	5	99.26% (0.02)	99.39% (0.01)	99.44%(0.02)	99.31% (0.02)	99.21%(0.02)	99.72%(0.01)
	7	99.06%(0.02)	99.21%(0.01)	99.39%(0.02)	99.10%(0.02)	99.03%(0.02)	99.67%(0.01)
	10	85.82%(0.06)	74.07%(0.08)	80.36%(0.06)	76.35%(0.09)	98.73%(0.03)	99.46%(0.02)
S2, 196	3	99.71% (0.01)	99.75% (0.01)	99.92% (0.01)	99.71% (0.01)	99.71% (0.01)	99.92% (0.01)
	5	99.37%(0.01)	99.53%(0.01)	99.82%(0.01)	99.36%(0.01)	99.37%(0.01)	99.82%(0.01)
	7	96.99%(0.10)	96.54%(0.13)	98.15%(0.08)	96.42%(0.13)	98.39%(0.04)	99.60%(0.01)
	10	90.84%(0.05)	85.81%(0.09)	85.67%(0.09)	84.48%(0.10)	99.03%(0.02)	99.57%(0.02)
S3, 120	3	98.62%(0.05)	98.36%(0.07)	98.88%(0.05)	98.03%(0.07)	99.55%(0.01)	98.88%(0.01)
	5	99.86% (0.01)	99.91% (0.01)	99.97% (0.01)	99.85% (0.01)	99.86%(0.01)	99.97%(0.01)
	7	99.33%(0.02)	99.57%(0.01)	99.75%(0.01)	99.50%(0.01)	99.19%(0.02)	99.75%(0.01)
	10	88.59%(0.11)	83.25%(0.17)	87.48%(0.12)	81.45%(0.18)	99.93% (0.01)	99.98% (0.01)
S3, 210	3	98.40%(0.06)	97.66%(0.09)	98.26%(0.07)	97.51%(0.09)	99.87%(0.01)	99.97%(0.01)
	5	99.47% (0.03)	99.22% (0.05)	99.42% (0.04)	99.17% (0.05)	99.96% (0.01)	99.99% (0.01)
	7	99.39%(0.03)	99.17%(0.05)	99.40%(0.04)	99.09%(0.05)	99.88%(0.01)	99.97%(0.01)
	10	90.35%(0.11)	85.46%(0.18)	88.42%(0.14)	84.77%(0.19)	99.56%(0.01)	99.90%(0.01)

B.5. Data and Code Availability

The California county temperature data is available at <https://www.ncei.noaa.gov/access/monitoring/climate-at-a-glance/statewide/time-series>. The adjectives and nouns data is available at <https://networks.skewed.de/net/adjnoun>. The code in this paper is available at <https://github.com/allenkei/GraphFL>.